Asymptotic normalization coefficients and the ^{7}Be$(p,\gamma)^8$B astrophysical S factor

A. Azhari,[1] V. Burjan,[2] F. Carstoiu,[3] C. A. Gagliardi,[1] V. Kroha,[2] A. M. Mukhamedzhanov,[1] F. M. Nunes,[4] X. Tang,[1] L. Trache,[1] and R. E. Tribble[1]

[1]*Cyclotron Institute, Texas A&M University, College Station, Texas 77843*
[2]*Institute for Nuclear Physics, Czech Academy of Sciences, Prague-Řež, Czech Republic*
[3]*Institute of Physics and Nuclear Engineering, Bucharest, Romania*
[4]*Universidade Fernando Pessoa, Praca 9 de Abril, 4200 Porto, Portugal*

We consider the results of two proton transfer reactions, ^{10}B$(^7$Be,^{8}B$)^9$Be and ^{14}N$(^7$Be,^{8}B$)^{13}$C, to obtain a weighted average of the measured asymptotic normalization coefficients for the virtual transition ^{7}Be $+p\leftrightarrow^8$B. These coefficients specify the amplitude of the tail of the ^{8}B overlap function in the ^{7}Be$+p$ channel, and are used to calculate the astrophysical S factor for the direct capture reaction ^{7}Be$(p,\gamma)^8$B at solar energies, $S_{17}(0)$. In light of recent improvements in the determination of optical-model potentials, including detailed understanding of the correlations between the DWBA analyses of the two experiments, and a new experimental measurement of the asymptotic normalization coefficients for the virtual transition ^{13}C$+p\leftrightarrow^{14}$N, we report a weighted average asymptotic normalization coefficient of $C_{p_{3/2}}^2=0.388\pm0.039$ fm^{-1} for ^{8}B $\leftrightarrow^7$Be$+p$, which implies $S_{17}(0)=17.3\pm1.8$ eV b.

I. INTRODUCTION

High-energy neutrinos from the β^+ decay of ^{8}B, produced in the ^{7}Be$(p,\gamma)^8$B reaction at solar energies ($\approx$20 keV), are the major source, if not all, of the observed neutrinos in existing and planned solar neutrino experiments (Homestake, Kamiokande, Super-Kamiokande, SNO, etc.) [1]. The observed deficit of ^{8}B neutrinos, when compared to solar model predictions, has focused much attention on the ^{7}Be$(p,\gamma)^8$B reaction rate, which is acknowledged as the most poorly known rate in the nucleosynthesis chain producing ^{8}B. Thus, the measurement of the ^{7}Be$(p,\gamma)^8$B reaction cross section at solar energies, or alternatively the astrophysical factor $S_{17}(0)$, is considered to be of high priority.

To date, six direct measurements of this cross section have been performed with quoted uncertainties of less than 10%. However, uncertainties involved in the use of radioactive ^{7}Be targets, together with extrapolation of the S factor to relevant energies, have proven challenging in these measurements. Each experiment provides a determination of $S_{17}(0)$ to $\sim$10%, but two of these results [2,3] are near 25 eV b, three [4–6] are near 18 eV b, while the most recent measurement [7] reports a value near 20 eV b. All of the experiments that measure excitation functions are consistent with the predicted energy dependence of $S(E)$ [8–11], indicating this discrepancy is due to unresolved problems in absolute normalizations. The most recent review of solar fusion rates adopted the value $S_{17}(0)=19^{+4}_{-2}$ eV b [12], making $S_{17}(0)$ the most uncertain input for solar model calculations. This review also emphasized the importance of indirect determinations of $S_{17}(0)$ that are sensitive to different systematic effects from those present in the direct cross-section measurements. Results from three indirect measurements, based on Coulomb dissociation of ^{8}B, have been reported [13–15]. However, the values of $S_{17}(0)$ from these measurements cover a broad range, roughly 13.5 to 22.2 eV b. Also, the

reliability of Coulomb dissociation to determine astrophysical S factors at stellar energies, to high accuracy, has not yet been verified [12].

At solar energies direct capture processes proceed through the tail of the nuclear overlap function [8], discussed in Sec. II. This is especially applicable to the ^{7}Be$(p,\gamma)^8$B reaction, given the very weakly bound proton in ^{8}B. For a fixed binding energy, at distances larger than the nuclear radius, the shape of this tail is determined by the Coulomb interaction, so the capture rate can be calculated accurately if one knows the amplitude of the tail. The asymptotic normalization coefficients (ANC) for ^{7}Be$+p\leftrightarrow^8$B specify the amplitude of the tail of the ^{8}B overlap function in the two-body channel when the ^{7}Be core and the proton are separated by a distance that is large compared to the nuclear radius. At these distances the overlap function is proportional to a Whittaker function, where the proportionality constant is the ANC. The ANC can be determined from measurements of nuclear reactions, such as peripheral nucleon transfer, where cross sections are orders of magnitude larger than the direct capture reactions themselves. Therefore, it provides a convenient approach to determine direct capture S factors at very low energies, including zero energy. In a previous study, this technique was tested by comparing directly measured S factors for ^{16}O$(p,\gamma)^{17}$F, for both the $5/2^+$ ground state and the $1/2^+$ first excited state, with those obtained from ANC's measured in the peripheral proton transfer reaction ^{16}O$(^3$He,$d)^{17}$F, and agreement of better than 9% was found [16]. More recently, good agreement was found in a comparison of the directly measured S factor for ^{12}C$(n,\gamma)^{13}$C*$(1/2^+,3.09$ MeV) with that obtained from the ANC measured in the ^{12}C$(d,p)^{13}$C* reaction [17].

An earlier experiment attempted to measure the ANC's for ^{7}Be$+p\leftrightarrow^8$B with the reaction ^{2}H$(^7$Be,^{8}B$)n$ [18]; however, interpretation of that experiment was complicated by uncertainties in the choice of optical-model parameters [19,20]. We have performed and reported, in two short pa-

pers, on two other indirect measurements based on determination of the ANC for $^7\text{Be}+p\leftrightarrow{}^8\text{B}$ from proton transfer reactions using a radioactive beam of ^7Be on ^{10}B [21] and ^{14}N targets [22], which reported values of 17.8 ± 2.8 eV b and 16.6 ± 1.9 eV b for $S_{17}(0)$, respectively. In the present paper we provide a more detailed presentation of the experiments and the methods used in obtaining the results. We also focus on obtaining a weighted average of these two measurements, taking into account recent improvements in the optical-model potentials [23] used in the distorted-wave Born approximation (DWBA) analysis and a detailed understanding of the correlations between the DWBA analyses of the two experiments in determining the ANC's.

II. ASYMPTOTIC NORMALIZATION COEFFICIENTS

Transfer reactions have been utilized extensively to extract spectroscopic factors. The analysis for these reactions has typically been carried out within the DWBA framework. It is known that the extracted spectroscopic factors often are strongly dependent on the geometric parameters of the Woods-Saxon potentials used to calculate the bound-state wave functions. For peripheral transfer reactions, the asymptotic normalization coefficient is another fundamental nuclear parameter that can be extracted, which is much less parameter dependent than the spectroscopic factor. Presented here is a short introduction to ANC's; a more detailed discussion can be found in Ref. [24].

Consider the transfer reaction

$$X+A\rightarrow Y+B, \tag{1}$$

where $X=Y+a$, $B=A+a$, and a is the transferred particle or cluster. The DWBA amplitude for this reaction is given by

$$M=\sum_{M_a} \langle \chi_f^{(-)} I_{Aa}^B(\mathbf{r}_{Aa})|\Delta V|I_{Ya}^X(\mathbf{r}_{Ya})\chi_i^{(+)}\rangle. \tag{2}$$

Here, $\chi_i^{(+)}$ and $\chi_f^{(-)}$ are the distorted waves in the initial and final channels, respectively, ΔV is the transition operator, and the sum is taken over the spin projections M_a. $I_{\beta\gamma}^\alpha(\mathbf{r}_{\beta\gamma})$ is the overlap function for the bound state $\alpha=(\beta\gamma)$, which includes radial and angular dependences. Usually the radial overlap function is approximated by a model wave function of the bound-state $\alpha=(\beta\gamma)$ written as

$$I_{\beta\gamma l_\alpha j_\alpha}^\alpha(r_{\beta\gamma})=S_{\beta\gamma l_\alpha j_\alpha}^{1/2}\varphi_{n_\alpha l_\alpha j_\alpha}(r_{\beta\gamma}). \tag{3}$$

Here $\varphi_{n_\alpha l_\alpha j_\alpha}(r_{\beta\gamma})$ is the bound state wave function of the relative motion of β and γ and $S_{\beta\gamma l_\alpha j_\alpha}$ is the spectroscopic factor of the configuration $(\beta\gamma)$ with quantum numbers l_α and j_α in nucleus α.

Given this standard substitution for the overlap functions, the conventional DWBA cross section is parametrized in terms of the spectroscopic factors of the initial and final nuclei and can be written as

$$\frac{d\sigma}{d\Omega}=\sum_{l_B j_B l_X j_X} S_{Aal_B j_B}S_{Yal_X j_X}\sigma_{l_B j_B l_X j_X}^{DW}, \tag{4}$$

where $\sigma_{l_B j_B l_X j_X}^{DW}$ is the reduced DWBA cross section that corresponds to the amplitude, Eq. (2), with overlap function given in Eq. (3), where $S_{\beta\gamma l_\alpha j_\alpha}=1$. However, in the case of peripheral transfer, the strong dependence of this reduced DWBA cross section on the geometric parameters r_0,a of the bound state Woods-Saxon potentials is a large source of uncertainty in the determination of the spectroscopic factors. Also, the spectroscopic factor is defined mainly by the behavior of the overlap function in the nuclear interior. Therefore, the parametrization of the DWBA cross section in terms of the spectroscopic factor for a peripheral reaction is not ideal. An alternative parametrization is the asymptotic normalization coefficient $C_{\beta\gamma l_\alpha j_\alpha}^\alpha$, which defines the amplitude of the tail of the overlap function $I_{\beta\gamma l_\alpha j_\alpha}^\alpha$:

$$I_{\beta\gamma l_\alpha j_\alpha}^\alpha(r_{\beta\gamma}) \xrightarrow{r_{\beta\gamma}>R_N} C_{\beta\gamma l_\alpha j_\alpha}^\alpha\frac{W_{-\eta_\alpha,l_\alpha+1/2}(2\kappa_{\beta\gamma}r_{\beta\gamma})}{r_{\beta\gamma}}, \tag{5}$$

where R_N is the nuclear interaction radius between β and γ, $W_{-\eta_\alpha,l_\alpha+1/2}(2\kappa_{\beta\gamma}r_{\beta\gamma})$ is the Whittaker function describing the asymptotic behavior of the bound-state wave function of two charged particles, $\kappa_{\beta\gamma}=\sqrt{2\mu_{\beta\gamma}\varepsilon_{\beta\gamma}}$ is the wave number of the bound state $\alpha=(\beta\gamma)$, $\mu_{\beta\gamma}$ is the reduced mass of particles β and γ, and $\eta_\alpha=Z_\beta Z_\gamma\mu_{\beta\gamma}/\kappa_{\beta\gamma}$ is the Coulomb parameter of the bound state $(\beta\gamma)$. The asymptotic behavior of the bound-state wave function has a similar form:

$$\varphi_{n_\alpha l_\alpha j_\alpha}(r_{\beta\gamma}) \xrightarrow{r_{\beta\gamma}>R_N} b_{\beta\gamma l_\alpha j_\alpha}\frac{W_{-\eta_\alpha,l_{\alpha+1/2}}(2\kappa_{\beta\gamma}r_{\beta\gamma})}{r_{\beta\gamma}}, \tag{6}$$

where $b_{\beta\gamma l_\alpha j_\alpha}$ is the single-particle ANC defining the amplitude of the tail of the bound-state wave function at large $r_{\beta\gamma}$. Equations (3), (5), and (6) imply

$$(C_{\beta\gamma l_\alpha j_\alpha}^\alpha)^2=S_{\beta\gamma l_\alpha j_\alpha}b_{\beta\gamma l_\alpha j_\alpha}^2. \tag{7}$$

Equation (7) is the key to a significant reduction of the dependence of the experimental results on the geometric parameters r_0,a of the bound-state Woods-Saxon potentials. The conventional DWBA analysis can be modified to take Eq. (7) into account by substituting this condition into Eq. (4) to obtain

$$\frac{d\sigma}{d\Omega}=\sum_{l_B j_B l_X j_X} (C_{Aal_B j_B}^B)^2(C_{Yal_X j_X}^X)^2 R_{l_B j_B l_X j_X}, \tag{8}$$

where we have defined R as

$$R_{l_B j_B l_X j_X}=\frac{\sigma_{l_B j_B l_X j_X}^{DW}}{b_{Aal_B j_B}^2 b_{Yal_X j_X}^2}. \tag{9}$$

R is practically insensitive to the bound-state potential parameters for peripheral reactions. Thus, the introduction of condition (7) guarantees the correct absolute normalization of the peripheral reaction cross section.

The ANC for $A+a\leftrightarrow B$, determined from a fit to peripheral transfer reaction data with Eq. (8), can then be used to

calculate the cross section for the direct radiative capture reaction $A+a\to B+\gamma$ at astrophysical energies. The direct capture amplitude is given by

$$M^{DC}=\lambda\langle I_{Aa}^{B}(\mathbf{r}_{Aa})|\hat{O}|\psi_{i}^{+}(\mathbf{r}_{Aa})\rangle, \tag{10}$$

where λ is a kinematic factor, I_{Aa}^{B} is the same overlap function that entered the DWBA amplitude for the peripheral transfer reaction, $\hat{O}$ is the electromagnetic transition operator, and ψ_{i}^{+} is the scattering wave function in the initial state. Note that Eq. (10) holds only for peripheral capture reactions. For a peripheral capture reaction at low energies, the incident scattering wave may be approximated by a pure Coulomb wave [8,16] and the overlap function may be replaced by its asymptotic form, Eq. (5). Thus, in this case, the direct capture rate is proportional to the square of the ANC, C_{Aa}^{B}.

For the specific case of $^{7}\text{Be}(p,\gamma)^{8}\text{B}$, the numerical relationship between $S_{17}(0)$ and the ^{8}B ANC's was derived in Ref. [8], which found

$$S_{17}(0)=\frac{38.6\ \text{eV b}}{\text{fm}^{-1}}[(C_{p_{3/2}}^{8_{B}})^{2}+(C_{p_{1/2}}^{8_{B}})^{2}]. \tag{11}$$

Alternative calculations that agree with this relation to within 2% may be found in Refs. [25,26].

Using the above analysis, the ANC, and hence the astrophysical S factor, can be determined from proton transfer reactions, with ^{7}Be as beam or target, at relatively large laboratory energies provided the transfer is peripheral. Of course, the technique described above can be generalized. Given the availability of radioactive beams, the ANC for radioactive systems can be obtained from transfer reactions using stable targets that have relatively large cross sections.

III. RADIOACTIVE BEAM PRODUCTION

In order to utilize the advantages of the ANC method, it is imperative that high intensity and high purity radioactive beams are available. At the Cyclotron Institute at Texas A&M University, radioactive beams are produced using transfer or fusion-evaporation reactions induced by a primary beam from the K500 superconducting cyclotron on a cryogenic gas target. The gas is contained in a 9-cm long cylindrical cell, placed in vacuum, with Havar windows. The thickness of the Havar foil can be varied to accommodate a range of beam energies and gas pressures. The gas cell is cooled with liquid nitrogen to obtain higher density at lower pressures, thus increasing the radioactive beam yield while minimizing the thickness of Havar needed. Degrader foils can be placed in front of the cell to degrade the primary beam energy. Similarly, foils can be placed behind the gas cell to further degrade the energy of the radioactive beam and to increase the charge state for high Z atoms.

Separation of radioactive beams is achieved using the Momentum Achromat Recoil Spectrometer (MARS) [27,28] shown in Fig. 1. MARS was designed for operation over a broad energy range with good mass resolution and high efficiency. Production of radioactive beams is achieved at 0°,
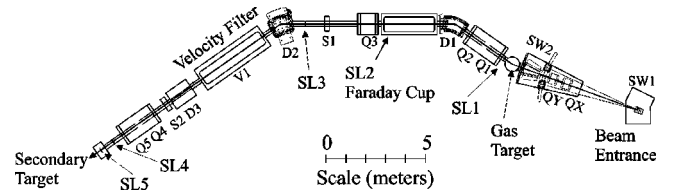

FIG. 1. Schematic diagram of the Momentum Achromat Recoil Spectrometer (MARS).

making use of inverse kinematics to increase particle yield at the focal plane. The optics of MARS were designed to have two dispersive planes. The first, which occurs right after the dipole magnet $D1$, provides a p/q dispersion in the horizontal direction with a maximum momentum dispersion at the entrance to the quadrupole magnet $Q3$. Momentum selection is achieved using horizontal slits (SL2) placed at a horizontal crossover of the beam in front of $Q3$. A Faraday cup is also positioned in front of $Q3$ to stop the primary beam and monitor its intensity. The quadrupole magnets $Q1$, $Q2$, and $Q3$ along with the dipole magnets $D1$ and $D2$ provide achromatic, nearly parallel transport of the radioactive beam into the velocity filter, where the beam is dispersed vertically. The dipole $D3$ is dispersion matched to the velocity filter such that it bends the beam up vertically, and together with quadrupoles $Q4$ and $Q5$ provides a first order M/q mass focus at the MARS focal plane.

Several recent improvements to MARS were implemented to improve the final purity and emittance of the radioactive beam. Horizontal and vertical slits (SL1) were placed directly behind the gas cell to adjust the angular acceptance into MARS. This helps to reduce the amount of beam halo at the focal plane, improving the final beam image by reducing the effects of higher-order aberrations that couple to θ and ϕ. Slits SL3 were added to reduce impurities due to scattering of lower velocity background beams from the bottom plate of the velocity filter. At the exit of $Q5$, the final magnetic element in MARS, two more sets of $x-y$ slits were placed, shown as SL4 and SL5 in Fig. 1. The M/q dispersion at the focal plane allows the use of the vertical components of SL5 to block impurities. Meanwhile SL4 and SL5 can be used to collimate the radioactive beam to optimize the beam-spot size and to fix the emittance on the secondary target.

Early radioactive beam experiments with MARS, including the $^{10}\text{B}(^{7}\text{Be},^{8}\text{B})^{9}\text{Be}$ experiment, exhibited a larger beam spot on the secondary target than anticipated from optics calculations. The sextupole $S2$ was originally configured to correct for second-order optical aberrations due primarily to dipole $D3$. However, a sextupole contribution from the dipole magnet in the Wien filter was found to be considerably larger than other second-order aberrations. This problem was corrected by rotating the sextupole $S2$ by 90°. Figure 2 shows a comparison of horizontal and vertical properties of the beam spots obtained before and after the sextupole correction for the ^{10}B and ^{14}N experiments, respectively. The overall effect of this modification was a tighter, more symmetric beam spot. In the case of the ^{7}Be radioactive beam, the beam spot was reduced from 3×6 mm^{2} (horizontal vs
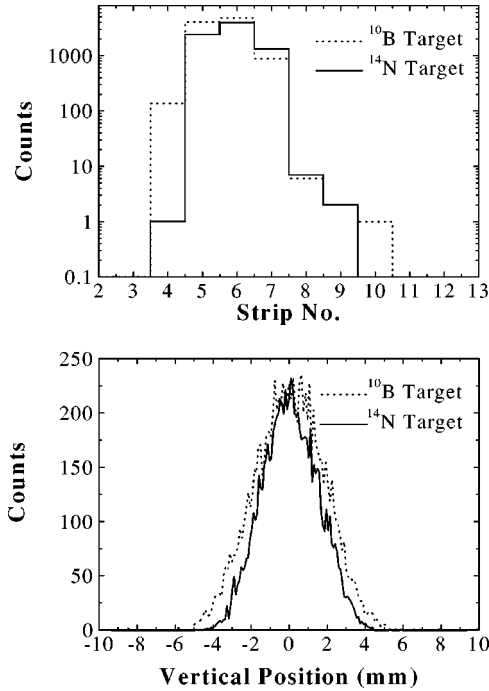
FIG. 2. Horizontal (upper panel) and vertical (lower panel) distributions of the ^{7}Be radioactive beam spot on target for the ^{10}B experiment, and for the ^{14}N experiment, after 90° rotation of sextupole $S2$.

vertical), in the ^{10}B(^{7}Be,^{8}B)^{9}Be experiment, to 2.5 $\times$3.6 mm^2 for the ^{14}N(^{7}Be,^{8}B)^{13}C experiment, all measured at full widths at half maxima.

IV. EXPERIMENTAL PROCEDURE

A ^{7}Be radioactive beam was produced via the reaction ^{1}H(^{7}Li,^{7}Be)n using a 135 MeV ^{7}Li^{+2} primary beam on the LN$_2$-cooled gas cell. The cell contained H$_2$ gas at slightly over 1 atm, to avoid any contamination from diffusion of air into the cell, corresponding to a target thickness of $\approx$3.6 mg/cm^2. Entrance and exit windows were made of Havar with a thickness of 42 mg/cm^2. A 69 mg/cm^2 Al degrader was placed in front of the gas cell to reduce the ^{7}Li beam energy, providing an 85 MeV radioactive beam of ^{7}Be at the focal plane of MARS.

A 5$\times$5 cm^2, 1000 μm thick, two-dimensional position-sensitive Si strip detector, shown in Fig. 3, was mounted on the target ladder and used for beam studies. This detector consisted of 16 independent resistive strips on the front and a common back plane readout. The horizontal position was determined from the strip number, while the vertical position was reconstructed from the charge division along the resistive strips. Total energy lost in the detector was determined from the back plane. Only 6 to 8 of the central strips of this detector were used due to the small size of the beam spot. In this configuration, particle identification was based on the correlation between the vertical position, which is dependent on the mass to charge ratio of the particle, and the total energy. In an alternate configuration, the above detector was replaced by a telescope consisting of a 100-μm silicon strip
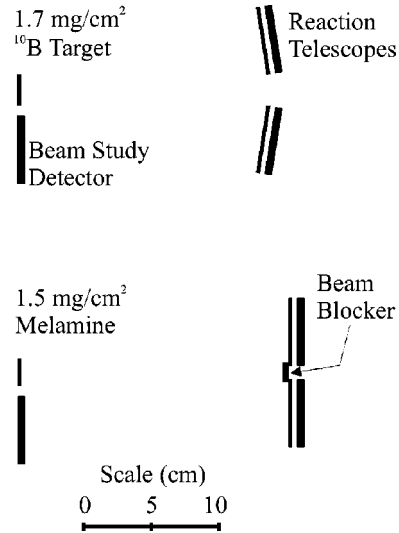
detector, backed by a 1000-μm 5$\times$5 cm^2 Si detector. In this telescope configuration, particle identification was accomplished by plotting particle energy against its position and/or energy loss against energy. Once particle identification was achieved, slits SL4 and SL5 were adjusted to block impurities. A purity of better than 99.4% was achieved, with α particles as the primary contaminants. Figure 4 shows the energy spectrum of particles at the target position. The α particles are indicated on the figure.

The energy spread of the beam was restricted to 1.6 MeV full width (FW) using the slits SL2 shown in Fig. 1. Beam emittance was optimized using the slits SL4 and SL5 in conjunction with each other to physically restrict beam dimensions. The angular profile of the beam was measured by closing SL4 to 5$\times$5 mm^2 and scanning across the beam distribution.

Another crucial function of the target detector was the measurement of the radioactive beam rate. A Faraday cup, located in the same chamber as the momentum slits (SL2), is used to stop the primary beam. The current measured in this Faraday cup can be calibrated against the target detector to indicate the number of radioactive beam particles seen at the
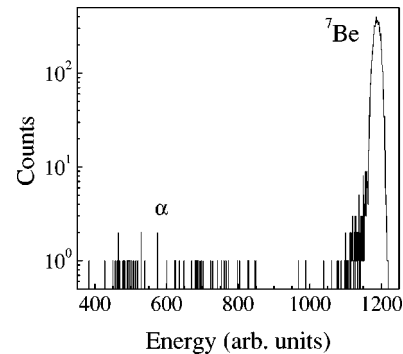
FIG. 3. Target and detector configuration for the ^{10}B experiment, upper panel, and the ^{14}N experiment, lower panel. Mass dispersion occurs in the vertical direction.

FIG. 4. Energy distribution of ^{7}Be radioactive beam on target detector. Also indicated is the 0.6% α impurity.

TABLE I. ^{7}Be beam properties.

	^{10}B target	^{14}N target
^{7}Li intensity	60 enA	150 enA
^{7}Be on target	50 kHz	80 kHz
Beam spot size ($H \times V$)	3×6 mm FWHM	2.5×3.6 mm FWHM
Angular spread ($H \times V$)	$4° \times 1.6°$ FW	$1.8° \times 0.6°$ FW
Energy spread	1.6 MeV FW	1.6 MeV FW

target position, allowing the measurement of the total number of radioactive beam particles by monitoring the Faraday cup. Periodic recalibration of the Faraday cup was made to check for any rate variations due to drifts in magnetic fields or beam heating of the H$_2$ gas in the cell. The rate variation was found to be less than 3% throughout both experiments. A list of beam properties for each experiment is presented in Table I. Taking advantage of the higher primary beam current and the modifications made to sextupole $S2$, the slits SL4 and SL5 were narrowed for the ^{14}N experiment. This improved the beam emittance considerably and explains the apparent inconsistency between the ratio of primary beam to secondary beam intensities in each experiment in Table I.

The target and detector assemblies were placed at the focal plane of MARS as shown in Fig. 3. Both elastically scattered ^{7}Be particles and proton transfer reaction products were observed simultaneously by two reaction telescopes. Each telescope consisted of a 5×5 cm^2, 105 μm thick Si ΔE detector, similar in orientation and readout to the target ladder detector, backed by a 1000 μm thick Si E detector. In order to minimize thermal noise in the detectors, the reaction telescopes were cooled to $-10°$ C by pumping refrigerated ethylene glycol through the detector housing assembly. Particle identification was achieved from the $\Delta E - E_{total}$ information. A sample identification spectrum is shown in Fig. 5, where good separation between different isotopes was achieved. Monte Carlo simulations, described in detail in Sec. V, were used to optimize the detector geometry for maximum geometric efficiency while minimizing physical damage from the ^{7}Be beam.

A prominent feature in Fig. 4 is the $\sim 1\%$ low energy tail of the ^{7}Be beam. This is primarily due to ^{7}Be beam particles that slit scatter at SL2 but remain within the normal acceptance of MARS. This was verified by observing the relative yields in the ^{7}Be full-energy peak and low-energy tail as the width of SL2 was adjusted. Beam halo particles that scatter from the edge of the target ladder are a source of background in the energy spectra. Therefore, a blank target frame was inserted in the target position and the fraction of the ^{7}Be beam in the halo was measured to be 2.7×10^{-5} and 1.3×10^{-4} for the ^{10}B and ^{14}N target experiments, respectively. This contribution was reduced by almost a factor of 2 by imposing a software gate on the elastically scattered ^{7}Be's in the $\Delta E - E_{total}$ spectra of each detector. No background ^{8}B events were observed off the blank target.

The self-supported ^{10}B target was produced by drying a slurry containing granules of enriched ^{10}B in a varnish on a Ta substrate. Distilled water was used to remove the layer of ^{10}B from the Ta. Based on auxiliary reaction studies, the ^{10}B

target was found to contain 77% ^{10}B, with ^{1}H, ^{11}B, ^{12}C, and ^{16}O as contaminants. The ^{14}N target consisted of evaporated melamine (C$_3$N$_6$H$_6$) supported by a 20 μg/cm^2 layer of C and a 20 μg/cm^2 layer of collodion. Target properties such as thickness and uniformity were verified using the radioactive ^{7}Be beam directly. The reaction telescopes were used to detect beam particles with and without the target. The resultant energy-loss measurement was then compared to results from the computer code SRIM [29]. The average thicknesses of the targets were 1.96 mg/cm^2 and 1.50 mg/cm^2 for the ^{10}B and ^{14}N targets, respectively. Instead of using simple Gaussian fits, a Monte Carlo simulation was written specifically to analyze the energy spectra. The energy shift, due to average target thickness, along with the broadening of the energy spectrum, was simulated to obtain the nonuniformity and straggling to within a few percent, the inherent accuracy of the code SRIM. Although the uniformity of the ^{14}N target was found to be better than 7%, the ^{10}B was found to have a significant thickness variation of up to 1.3 mg/cm^2 due to the grain size used in the slurry. However, the uncertainty in the final result, due to this nonuniformity, is minimal since all beam parameters, except intensity, were kept the same during the test measurements as they were during the actual data collection. Overall, the absolute normalizations of the
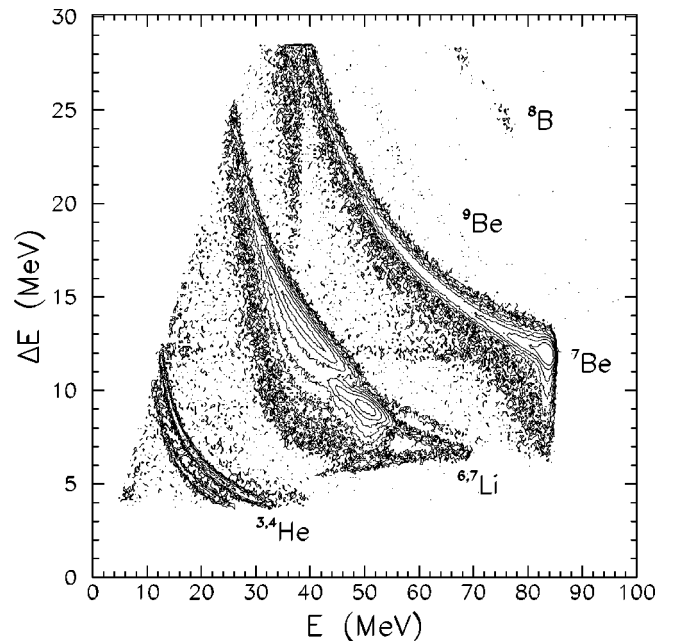

FIG. 5. Particle identification plot of energy loss versus total energy.

cross sections were determined to 6.4% and 5.0% for the ^{10}B and ^{14}N targets, respectively.

The detector signals were processed using standard analog electronics and CAMAC modules, with a VME controller. Data were recorded and analyzed on-line using the code XSYS [30]. Due to the small event rate, shown in Table I, data were written directly on disk for off-line analysis.

Position calibration of the ΔE detectors was accomplished using a specially constructed mask consisting of five horizontal 1-mm slits at 8-mm intervals for each detector. In the final configuration, this mask was mounted on the detector housing assembly, at a distance of about 1 mm from the surface of the detector. Both α particles from a ^{228}Th source and the ^{7}Be radioactive beam were used to illuminate the slits, providing two different particles to determine and verify the position calibration parameters.

The α source and ^{7}Be beam were also used to obtain energy calibrations for both the ΔE and E detectors. Due to the small energy of the α particles, compared to that of the beam, the energy calibration obtained for the E detectors were refined further using the methods described in the next section.

V. DATA ANALYSIS AND SIMULATION

The position and energy information from the detector telescopes were used to perform a kinematic reconstruction of the reaction and to obtain the Q-value spectra for both elastic and transfer reactions. Although most observables such as distances and angles were physically measured in the laboratory, refinement of these measurements, including energy calibrations, were performed utilizing the data events. The large sensitivity of the Q value on experimental observables was exploited to optimize the setup parameters and their respective uncertainties. Position gates were applied in the software to divide each reaction telescope into several regions, and Q-value spectra for elastic and transfer reactions were created for each region. The Q values for these reactions are well known, allowing a minimization process to be applied to obtain the optimum setup parameters and their uncertainties. This method is especially useful when applied to elastically scattered particles due to the large statistics and high sensitivity of the distribution across the detector surface to beam and detector parameters. These optimized values were then used in the experimental kinematic reconstruction and also as input parameters for the Monte Carlo simulations.

A detailed Monte Carlo simulation code was written specifically for the experimental setup described in Sec. IV. The code was written to include three main effects: beam properties, target effects, and detection mechanisms.

Simulation of the beam required two main sets of parameters, physical characteristics and energy distribution, which were obtained during the experiment. The beam trajectory and emittance were measured during the slit scans. The trajectory was approximated by a central vector with an appropriate distribution describing the spread around it matching the beam-spot size and location on the target detector. The magnetic fields in the dipole elements $D1$ and $D2$, calculated from current settings, were used to calculate the rigidity of the transmitted particles, and thus, the mean beam energy. The momentum spread was then calculated from the opening in slit SL2 and verified by the beam studies detector.

Target effects included the energy loss of the ^{7}Be particles entering the target, interaction of the beam with the target (i.e., elastic scattering or transfer reaction), and the energy loss of the exiting particle. Stopping power calculations, using the code SRIM, were performed to obtain the mean energy loss per mg/cm^2 of target material as a function of particle energy for both beam particles and reaction products. Fit parameters relating the energy loss to particle energy were obtained from these calculations and included in the simulation. Thus, the simulation could calculate the correct energy loss for the appropriate particle as a function of particle energy and path of travel through the target medium both before and after the reaction. Straggling effects, also calculated using SRIM, were much smaller than the inherent resolutions and, thus, were neglected. The thickness variation of the targets, especially important in the case of the ^{10}B target, also contributes to target effects and was incorporated in the simulation code. Differential cross sections for the elastic scattering and transfer reactions were obtained using the methods described in the following sections and input to the simulations. These cross sections were used to simulate the scattering angle in the center of mass, which was then converted to the laboratory frame using relativistic kinematics. Accounting for energy losses in the target, a final momentum vector was obtained which defined the velocity and direction of the particle exiting the target. Effects due to multiple scattering were ignored since this contribution is negligible compared to uncertainties in absolute normalization.

The detector geometry was incorporated based on parameters describing the detector that were read from an input file. The primary geometric parameters for the detector assembly, shown in Fig. 3, were distance from target, distance from beam axis, detector angle, and offset in the horizontal plane relative to the beam. Total-energy resolution and position resolution were also included in the detection simulation. This allowed us to obtain the experimental observables, i.e. position and energy, convoluted with experimental resolutions and efficiencies, and to employ the same experimental analysis routines to reconstruct angular distributions and Q-value spectra.

With the Monte Carlo simulation parameters calibrated, detector solid angles can be determined as a function of scattering angle, including all experimental resolutions. This was achieved by inputting a flat angular distribution into the simulation using the experimental set of simulation parameters. By extracting the experimental cross section as a function of the scattering angle, using the same angular bins as in the simulation, the experimental differential cross section can be obtained and compared with theoretical calculations.

VI. OPTICAL-MODEL POTENTIALS

Optical-model parameters are typically obtained from fits to elastic-scattering angular distributions. However, a precise

determination of the elastic-scattering angular distribution is not always possible, especially for radioactive beams. Therefore, a search for optical-model potentials to describe elastic scattering and transfer reactions involving loosely bound stable and radioactive p-shell nuclei, was performed [23]. The elastic-scattering angular distributions of ^{7}Be were predicted using optical-model parameters obtained from double folding model calculations convoluting Hartree-Fock density distributions with the effective interaction of Jeukenne, Lejeune, and Mahaux [31]. The folded potentials were renormalized to match the systematics observed in the elastic scattering of p-shell nuclei around 10 MeV/nucleon—including ^{7}Li+^{9}Be (at two energies), ^{7}Li+^{13}C (at two energies), ^{10}B+^{9}Be [24], ^{13}C+^{9}Be, and ^{14}N+^{13}C [32]. Thus, seven angular distributions were measured to obtain the renormalization factors needed to fit elastic scattering in this mass region. The renormalization factors are found to be nearly independent of the colliding system, minimizing the uncertainties due to the choice of optical potentials.

In a previous calculation, the uncertainties in assessing the depths of the potentials in the entrance and exit channels for the ^{10}B(^{7}Be,^{8}B)^{9}Be reaction were treated as totally correlated, resulting in an overall uncertainty of 10% [21]. A more detailed study of this uncertainty was performed recently [23]. In order to estimate the uncertainty in the ANC's due to the optical-model potentials, we use the standard deviations of the renormalization coefficients from the folding model fits, which provide a good measure of the sensitivity in the determination of the real and imaginary potential wells. By the choice of the systems considered above, we span a good range of p-shell nuclei, averaging properties similar to those of radioactive ones. The standard deviations around the average value of the renormalization coefficients were used to evaluate the uncertainty in extracting the ANC's, which arise through the DWBA calculations of the transfer reaction cross section. The potential depths were varied over a 1σ range of deviations of the renormalization coefficients for the real and imaginary parts independently in the entrance and exit channels. The resulting variations were then added in quadrature to estimate the relative uncertainty in the DWBA calculations. With this procedure an 8.1% uncertainty in the calculated transfer cross sections, due to the DWBA, was obtained. Note that in varying the depths of the potentials in the entrance and exit channels separately for the same reaction, the uncertainties are treated as uncorrelated between the channels involving ^{7}Be and ^{8}B, respectively. However, the uncertainties between the two different reactions remain correlated through the use of the same procedure and of the same average values for the renormalization coefficients.

Optical potentials for the elastic scattering of the ^{7}Be beam were obtained, using the above recipe, for the ^{10}B and melamine targets, including all contaminants and components. These were then used to calculate the differential cross section for the elastic scattering. Differential cross sections were calculated for the elastic scattering of ^{7}Be on H, B, C, N, and O. These angular distributions were used to simulate the Q-value spectra for the elastic scattering. Figure 6 shows comparisons, not fits, of the simulated Q-value spectra to the
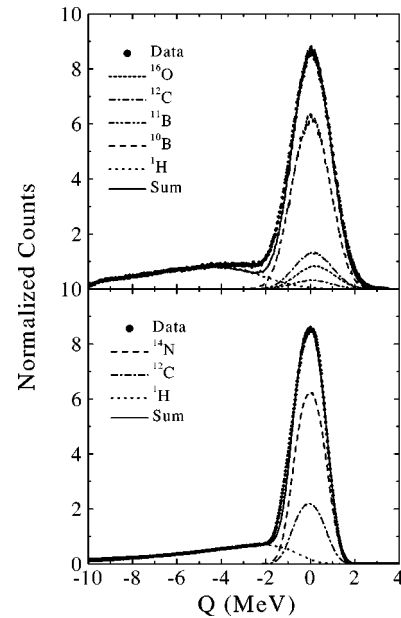

FIG. 6. Q-value spectra for the elastic scattering of ^{7}Be on the boron, upper panel, and melamine, lower panel, targets. The solid line is a sum of contributions from all nuclei present in each target.

data for the elastic scattering of ^{7}Be on the ^{10}B target, upper panel, and the melamine target, lower panel. Also shown are the separate contributions from the various components in each target, where the relative normalization was fixed to the actual abundances of each atomic species, and the absolute normalization was calculated from measured beam intensity and target density. The contributions from inelastic scattering were not included in the simulations, which accounts for the slight excess of data at about -2 MeV. However, this is a minor effect and good agreement is obtained to well beyond the energy region of interest.

By using a flat angular distribution in the Monte-Carlo simulation, the solid angle was obtained for each elastic-scattering data bin using the kinematics for ^{10}B and ^{14}N for the two targets. Elastic scatterings from contaminants were analyzed assuming scattering from the target nuclei since they could not be distinguished in the experiment. The simulated solid angles were then summed to obtain a total angular distribution for each target. This procedure yielded a total theoretical elastic-scattering angular distribution smoothed by all experimental resolutions, contained within the simulated solid angles. Figure 7 shows comparisons, not fits, of the angular distributions obtained for elastic scattering of ^{7}Be on the ^{10}B target (including impurities of ^{12}C and ^{16}O) [21], upper panel, and on the ^{14}N target (including impurities of ^{12}C and ^{1}H) [22], lower panel, to distributions calculated using the above prescription. Contributions to the angular distribution from inelastic scattering and the scattering off of hydrogen in the targets was minimized by setting a lower limit of -1.4 MeV and -1.2 MeV on the Q value for ^{10}B and ^{14}N targets, respectively, in both the data and simulations. There is good agreement, especially since the calculations do not include contributions from inelastic scattering populating the ^{7}Be first excited state, which is not resolved
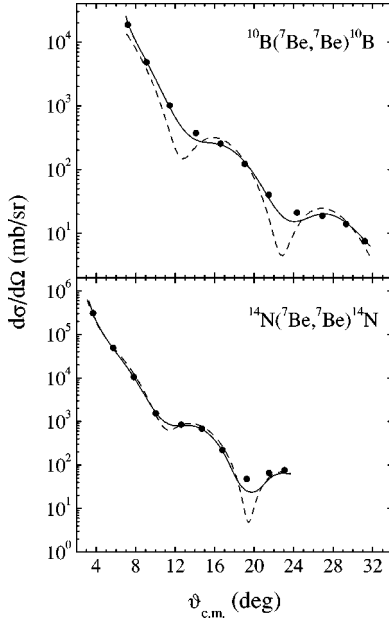
FIG. 7. Observed ^{7}Be elastic-scattering angular distributions for ^{10}B and ^{14}N targets, shown as solid circles. The dashed curves are the predicted angular distributions, summed over all target nuclei, while the solid curves show the same distributions corrected for finite angular resolution.

from the elastic scattering. High-resolution elastic-scattering studies in this energy region involving ^{7}Li projectiles [23] imply that these excited states should contribute less than 15% of the total yield observed near the elastic-scattering minima, and less than 1% at the maxima. This explains the larger yield observed in the minima of the data relative to the predicted cross section. Away from the minima, the ratios of predicted cross sections to data vary from unity by an average of less than 3%, well within the overall normalization uncertainty in our measured cross sections.

VII. ANC AND $S_{17}(0)$

The ANC specifies the amplitude of the tail of the overlap function in the two-body channel when the core and the proton are farther apart than the nuclear radius. For peripheral transfer reactions ANC's are extracted from the measured cross section by comparison to a DWBA calculation. In the ^{10}B(^{7}Be,^{8}B)^{9}Be(g.s.) reaction, the $p_{3/2}$ proton in the ground state of ^{10}B transfers to either the $p_{1/2}$ or $p_{3/2}$ orbitals constituting the ground state of ^{8}B. The experimental cross section for this transfer is given by [21]

$$\frac{d\sigma}{d\Omega} = \frac{(C^{^{10}\mathrm{B}})^2}{(b^{^{10}\mathrm{B}})^2}\left[\frac{(C^{^8\mathrm{B}}_{p_{3/2}})^2}{(b^{^8\mathrm{B}}_{p_{3/2}})^2}\sigma^{DWBA}_{p_{3/2}} + \frac{(C^{^8\mathrm{B}}_{p_{1/2}})^2}{(b^{^8\mathrm{B}}_{p_{1/2}})^2}\sigma^{DWBA}_{p_{1/2}}\right]. \tag{12}$$

The experimental cross section for the ^{14}N(^{7}Be,^{8}B)^{13}C(g.s.) reaction is similar to Eq. (12), except there are four terms arising from the transfer of the proton in the ground state of ^{14}N occupying either a $p_{1/2}$ or a $p_{3/2}$ orbital [22]. As evident from Eq. (12), calculation of the ANC's for ^{8}B requires the
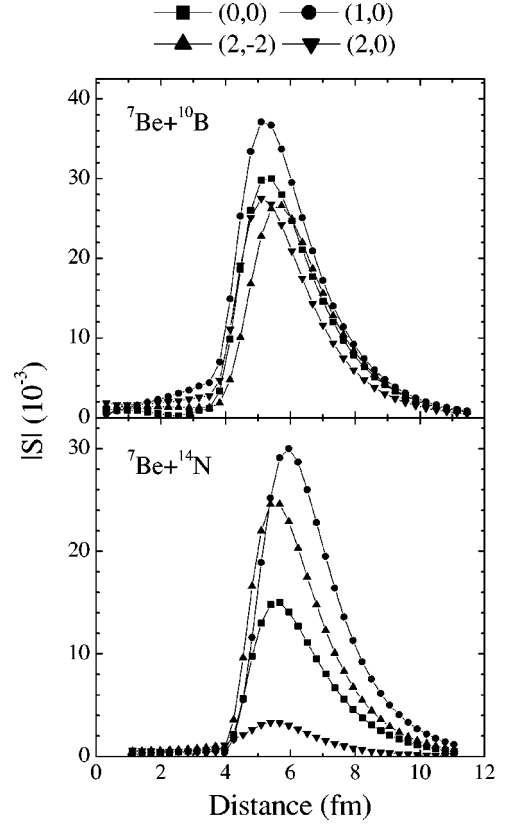

FIG. 8. *S*-matrix calculations for the transfer reactions as a function of separation distance. Calculations were performed for several values of $(L_X,\Delta l)$, where $\mathbf{L}_X \equiv \mathbf{l}_{Projectile} - \mathbf{l}_{Target}$ and $\Delta l \equiv \mathbf{L}_{Exit} - \mathbf{L}_{Entrance}$.

ANC's for the complementary vertices. They have been reported as $C^2_{p_{3/2}}(^{10}\mathrm{B}) = 4.91 \pm 0.37$ fm^{-1} [23,24], from a study of the ^{9}Be(^{10}B,^{9}Be)^{10}B, $C^2_{p_{1/2}}(^{14}\mathrm{N}) = 18.2 \pm 0.9$ fm^{-1} and $C^2_{p_{3/2}}(^{14}\mathrm{N}) = 0.91 \pm 0.14$ fm^{-1} from complementary studies of the ^{13}C(^{14}N,^{13}C)^{14}N [32] and ^{13}C(^{3}He,d)^{14}N [33] reactions. DWBA calculations were carried out with the finite-range code PTOLEMY [34], using the full transition operator. In each case, the distorted waves for the entrance channel were calculated with the folding model optical potential used in the elastic-scattering calculations above, while the exit channel optical potentials were derived from a similar folding model calculation.

Since ANC's were extracted from the angular distributions, checks were made for both transfer reactions used in the experiments to insure that they were peripheral. The *S*-matrix was calculated to verify the peripheral nature of the reactions. Figure 8 shows the results of this calculation as a function of the separation distance between the two colliding nuclei, obtained from the semiclassical relationship between angular momentum and distance. The maxima in these calculations occur at 5.2 fm and 5.8 fm for the ^{7}Be$+^{10}$B and ^{7}Be$+^{14}$N reactions, respectively. For both cases, these distances are larger than the sum of the radii, 4.9 fm and 5.2 fm, respectively, indicating that the reactions are indeed peripheral.

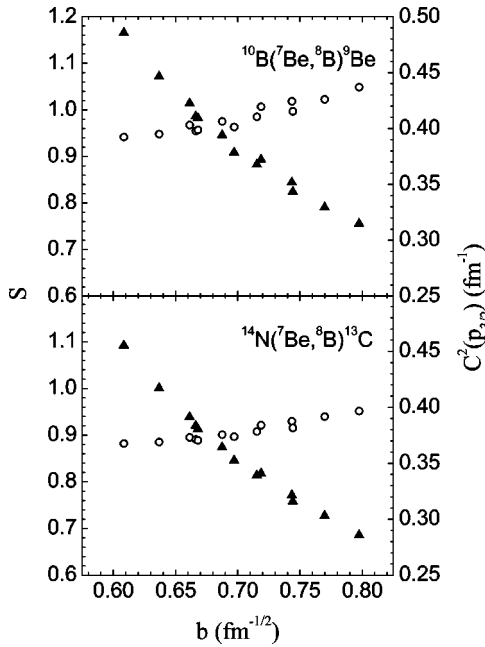Although the *S*-matrix calculations are a good indication

FIG. 9. Comparison of variation of calculated spectroscopic factors (triangles, left axis) and the ANC's (circles, right axis), obtained for different values of well radius and diffusivity for each target.
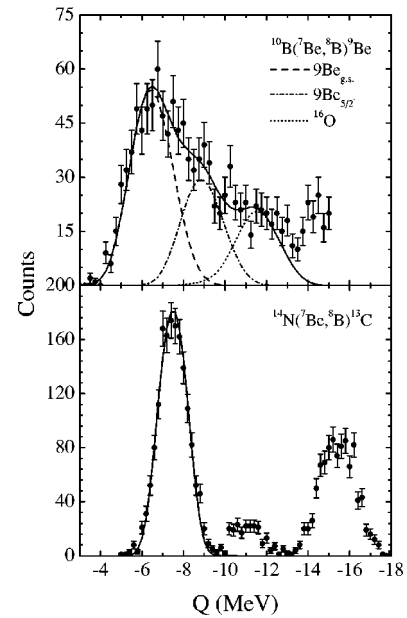

FIG. 10. Q-value spectra of the outgoing ^{8}B nuclei. The solid curves are Monte Carlo simulations normalized to the data. Also shown are the different components used to fit the Q-value spectrum obtained for the ^{10}B target.

of the peripheral character of a transfer reaction, they do not indicate the sensitivity of the ANC to the parameters of the DWBA calculations. Therefore, a more refined test is needed. The most stringent test of sensitivity is obtained by observing the stability of the extracted ANC when varying the parameters of the single-particle Woods-Saxon potential wells. Figure 9 shows a comparison of the inferred spectroscopic factor and ANC for the dominant $p_{3/2}$ orbital in ^{8}B as a function of the single-particle ANC, b, for both transfer reactions considered in this paper. These values were obtained by varying the single-particle Woods-Saxon well parameters r_0 and a within a realistic range of values, 1–1.3 fm and 0.5–0.7 fm, respectively. As evident from Fig. 9, the values obtained for the calculated spectroscopic factor cover a range 4 to 6 times larger than the ANC.

Angular distributions predicted from DWBA calculations were obtained for the reactions ^{10}B(^{7}Be,^{8}B)^{9}Be and ^{14}N(^{7}Be,^{8}B)^{13}C using optical-model potentials found by the prescription discussed in Sec. VI. These DWBA cross sections were input to the Monte Carlo simulation using the same experimental input parameters that provided excellent fits to the elastic scattering. Figure 10 shows fits of the angle-integrated Q-value spectra for the outgoing ^{8}B nuclei with simulations of the transfer reactions for both targets. In the case of the ^{10}B target, contributions from the second excited state of ^{9}Be and ^{16}O contamination in the target were also simulated and included in the summed spectra since these contributions could not be separated from the ground-state transfer due to experimental energy resolution. A three parameter χ^2 minimization was used to provide the best fit to the measured Q-value spectrum over the range -4 MeV $>Q>-12$ MeV. Figure 10 also shows ^{8}B yield beyond -12 MeV, for the ^{10}B target, from population of higher

excited states in ^{9}Be and reactions off the ^{12}C in the target. These states were not included in the Q-value fit as they have a negligible impact on the normalization of the cross sections of interest. Using the measured target thickness, the absolute number of ^{7}Be beam particles, and the normalization from Q-value fits, the total experimental cross sections for populating the ^{9}Be and ^{13}C ground states were calculated to be 1.40 ± 0.13 mb and 1.131 ± 0.066 mb, respectively.

The calculated DWBA angular distributions were also compared to the data, shown in Fig. 11, using the same normalization factors obtained from the Q-value fits. In the case of the ^{10}B(^{7}Be,^{8}B)^{9}Be reaction, contributions to the angular distribution from excited states and contaminants in the ^{10}B target were minimized by considering events with $Q>-7.5$ MeV for data analysis and simulations.

The predicted angular distributions in Fig. 11 assume the proton transfer occurs as a direct, one-step process. In order to estimate the impact of possible multistep effects on our extracted ANC's, we have performed coupled-channels Born-approximation calculations of the ^{10}B(^{7}Be,^{8}B)^{9}Be reaction with the code FRESCO [35]. We chose this reaction since ^{9}Be and ^{10}B, being located in the middle of the $1p$ shell, are significantly deformed. In addition to the ground states of ^{9}Be and ^{10}B, the calculation included the $5/2^-$ and $7/2^-$ states of ^{9}Be at 2.43 and 6.76 MeV and the 4^+ state in ^{10}B at 6.03 MeV. Spectroscopic amplitudes for the various proton transfers and deformation parameters for the inelastic excitations were taken from Ref. [36]. For the latter, we adopted the larger of the two sets of deformation parameters in Ref. [36] in order to obtain an upper limit on the expected effects. These calculations show that the predicted small-angle ^{10}B(^{7}Be,^{8}B)^{9}Be cross section changes by less than 4% when the coupled channels are included, and the largest pre-
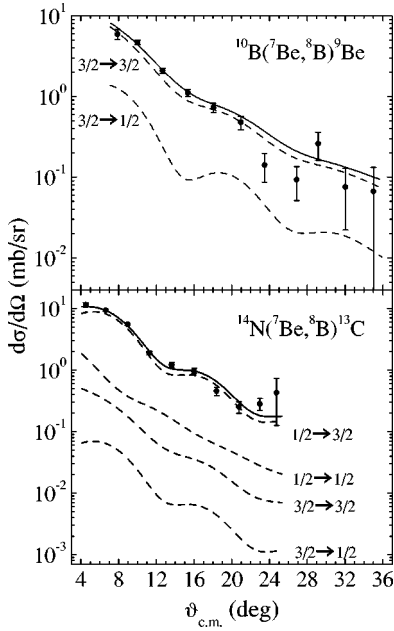
FIG. 11. Fit of the measured transfer reaction angular distributions. The dashed lines were obtained from DWBA calculations for the individual proton orbital angular momentum transfers. They were summed to obtain the total predicted angular distributions (solid), normalized to the total cross sections inferred from the Q-value fits in Fig. 10. All curves have been corrected for finite angular resolution.

dicted deviation over the angular range for which we have good statistics is approximately 20%. If we fit our measured angular distribution with the coupled-channels prediction, the extracted $^7\text{Be}+p \leftrightarrow {}^8\text{B}$ ANC's change by 3.5%. Further, reducing one of the spectroscopic amplitudes by a factor of 2 yield ANC's from the coupled-channels prediction that agree with the DWBA results to within 0.5%. From this, we conclude that the impact of multistep effects on the measured ANC's is small. We have included a 3% contribution to the uncertainties to account for this effect. A more detailed investigation of coupled-channel effects, including channel coupling in the $^7\text{Be} - {}^8\text{B}$ system and a full study of $^{14}\text{N}(^7\text{Be},{}^8\text{B})^{13}\text{C}$, will be the subject of a future publication.

The relation between ANC's and cross sections, i.e., Eq. (12) and its equivalent equation for ^{14}N, can be used to extract the ANC's for ^8B. However, individual contributions from the $p_{3/2}$ and $p_{1/2}$ orbitals in the ground state of ^8B could not be disentangled to determine the ANC $C^2_{p_{1/2}}$. Therefore, microscopic calculations were employed to determine the ratio $C^2_{p_{1/2}}/C^2_{p_{3/2}}$ to be 0.157 [37], resulting in $C^2_{p_{3/2}}$ values for the $^7\text{Be}+p \leftrightarrow {}^8\text{B}$ reaction of 0.410 ± 0.055 fm^{-1} and 0.379 ± 0.042 fm^{-1} for the ^{10}B and ^{14}N targets, respectively. Equation (1) was then applied using these ANC's to obtain $S_{17}(0) = 18.4 \pm 2.5$ eV b and $S_{17}(0) = 16.9 \pm 1.9$ eV b for the $^{10}\text{B}(^7\text{Be},{}^8\text{B})^9\text{Be}$ and $^{14}\text{N}(^7\text{Be},{}^8\text{B})^{13}\text{C}$ reactions, respectively.

In order to obtain a weighted average of the two values of $S_{17}(0)$ reported above, a detailed consideration of all degrees of correlation within the uncertainties of the two values was

TABLE II. Contributions to the uncertainties in $S_{17}(0)$.

	$^{10}\text{B}(^7\text{Be},{}^8\text{B})^9\text{Be}$	$^{14}\text{N}(^7\text{Be},{}^8\text{B})^{13}\text{C}$
Statistical	3.9%	2.5%
Monte Carlo	2.4%	1.4%
Absolute normalization	6.4%	5.0%
ANC of second vertex	7.6%	4.9%
DWBA	8.1%	8.1%
Multistep effects	3.0%	3.0%
Total	13.6%	11.2%

undertaken. No correlation in the statistical uncertainties is expected since the two experiments were performed independently. Similarly, the Monte Carlo simulation parameters were calibrated to the elastic-scattering data individually for each experiment, hence, uncertainties due to the choice of simulation parameters were independent for each experiment and no correlations should exist. However, the choice of optical-model parameters for the elastic scattering and, in turn, for the transfer reactions was derived using the same methods described in Sec. VI. Therefore, a 100% correlation for the uncertainties in the DWBA calculations was adopted. A detailed account of the uncertainties in each experiment is presented in Table II. Including the 100% correlation in the optical-model calculations into the averaging process, we obtain weighted average values of $C^2_{p_{3/2}} = 0.388 \pm 0.039$ fm^{-1} and $S_{17}(0) = 17.3 \pm 1.8$ eV b. Figure 12 presents a chronological compilation of reported value for $S_{17}(0)$, including direct reactions, Coulomb dissociations, and ANC methods. As can be seen in this figure, our result for $S_{17}(0)$ is in good agreement with the current adopted value of $S_{17}(0) = 19^{+4}_{-2}$ eV b [12]. Furthermore, it is consistent with the most recently reported values of $S_{17}(0)$ from both direct reaction [7] and Coulomb dissociation [15] experiments.
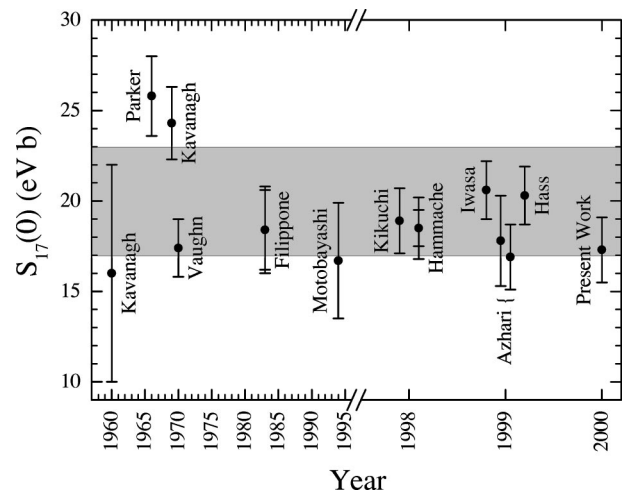

FIG. 12. Time-line compilation of experimental results reported for $S_{17}(0)$ identified using first author's names in chronological order: Kavanagh [38], Parker [2], Kavanagh [3], Vaughn [4], Filippone [5], Motobayashi [13], Kikuchi [14], Hammache [6], Iwasa [15], Azhari [21,22], Hass [7], and present result. The shaded region represents the current adopted range for $S_{17}(0)$ [12].

VIII. CONCLUSIONS

The asymptotic normalization coefficient for the virtual transition $^7Be+p\leftrightarrow{}^8B$ was measured from the proton transfer reactions $^{10}B(^7Be,{}^8B)^9Be$ and $^{14}N(^7Be,{}^8B)^{13}C$ and used to extract the astrophysical $S_{17}(0)$ factor in previous publications [21,22]. These results were reanalyzed in light of recent experimental results and refinements in the optical-model analysis and DWBA calculations.

In the original analysis of the $^{10}B(^7Be,{}^8B)^9Be$ reaction, the choice of optical-model potentials used to calculate the ANC for the capture reaction $^9Be+p\rightarrow{}^{10}B$ was obtained by a weighted average [24]. However, this choice has since been narrowed down to only one potential [23]. Also, a more in-depth analysis of uncertainties due to DWBA calculations allowed a reduction in this uncertainty. Incorporating these new findings into the calculations for the $^{10}B(^7Be,{}^8B)^9Be$ reaction yields a new value of $S_{17}(0)=18.4\pm2.5$ eV b. This corresponds to a 3.4% increase in the value of the S factor, while the uncertainty has been reduced from 15.7% to 13.6%.

The ANC for the $^{13}C+p\rightarrow{}^{14}N$ reaction has been measured in a recent study and folded with a previous measurement to obtain a weighted average [33]. Incorporating this result into the analysis of the $^{14}N(^7Be,{}^8B)^{13}C$ reaction resulted in an increase of 1.8% in the measured value of $S_{17}(0)$ and a reduction of its uncertainty. This new result, along with the reduction in uncertainty from the DWBA calculations, were included to obtain $S_{17}(0)=16.9\pm1.9$ eV b for the $^{14}N(^7Be,{}^8B)^{13}C$ reaction.

An analysis of correlations in the uncertainties due to the DWBA analysis was performed in order to obtain a weighted average for the two values of $S_{17}(0)$ presented above. Incorporating the 100% correlation within the DWBA uncertainties into the weighted average gives $S_{17}(0)=17.3\pm1.8$ eV b.

[1] J. N. Bahcall, in *Solar Modeling* (World Scientific, Singapore, 1994), p. 1, and references cited therein.

[2] P. D. Parker, Phys. Rev. **150**, 851 (1966).

[3] R. W. Kavanagh, T. A. Tombrello, J. M. Mosher, and D. R. Goosman, Bull. Am. Phys. Soc. **14**, 1209 (1969).

[4] F. J. Vaughn, R. A. Chalmers, D. Kohler, and L. F. Chase, Phys. Rev. C **2**, 1657 (1970).

[5] B. W. Filippone, A. J. Elwyn, C. N. Davids, and D. D. Koetke, Phys. Rev. Lett. **50**, 412 (1983); Phys. Rev. C **28**, 2222 (1983).

[6] F. Hammache *et al.*, Phys. Rev. Lett. **80**, 928 (1998).

[7] M. Hass *et al.*, Phys. Lett. B **462**, 237 (1999).

[8] H. M. Xu, C. A. Gagliardi, R. E. Tribble, A. M. Mukhamedzhanov, and N. K. Timofeyuk, Phys. Rev. Lett. **73**, 2027 (1994).

[9] P. Descouvemont and D. Baye, Nucl. Phys. **A567**, 341 (1994).

[10] A. Csoto, Phys. Lett. B **394**, 247 (1997).

[11] P. Descouvemont and D. Baye, Phys. Rev. C **60**, 015803 (1999).

[12] E. G. Adelberger *et al.*, Rev. Mod. Phys. **70**, 1265 (1998).

[13] T. Motobayashi *et al.*, Phys. Rev. Lett. **73**, 2680 (1994).

[14] T. Kikuchi *et al.*, Eur. Phys. J. A **3**, 213 (1998).

[15] N. Iwasa *et al.*, Phys. Rev. Lett. **83**, 2910 (1999).

[16] C. A. Gagliardi *et al.*, Phys. Rev. C **59**, 1149 (1999).

[17] N. Imai *et al.*, in Proceedings of the Conference on Nuclei in the Cosmos, Aarhus, Denmark, 2000, edited by J. Christensen-Dalsgaard and K. Langanke (unpublished).

[18] W. Liu *et al.*, Phys. Rev. Lett. **77**, 611 (1996).

[19] C. A. Gagliardi, A. M. Mukhamedzhanov, R. E. Tribble, and H. M. Xu, Phys. Rev. Lett. **80**, 421 (1998).

[20] J. C. Fernandes, R. Crespo, F. M. Nunes, and I. J. Thompson, Phys. Rev. C **59**, 2865 (1999).

[21] A. Azhari, V. Burjan, F. Carstoiu, H. Dejbakhsh, C. A. Gagliardi, V. Kroha, A. M. Mukhamedzhanov, L. Trache, and R. E. Tribble, Phys. Rev. Lett. **82**, 3960 (1999).

[22] A. Azhari, V. Burjan, F. Carstoiu, C. A. Gagliardi, V. Kroha, A. M. Mukhamedzhanov, X. Tang, L. Trache, and R. E. Tribble, Phys. Rev. C **60**, 055803 (1999).

[23] L. Trache, A. Azhari, F. Carstoiu, H. L. Clark, C. A. Gagliardi, Y.-W. Lui, A. M. Mukhamedzhanov, and R. E. Tribble, Phys. Rev. C **61**, 024612 (2000).

[24] A. M. Mukhamedzhanov, *et al.*, Phys. Rev. C **56**, 1302 (1997).

[25] B. K. Jennings, S. Karataglidis, and T. D. Shoppa, Phys. Rev. C **58**, 3711 (1998).

[26] A. Csoto, Phys. Rev. C **61**, 037601 (2000).

[27] R. E. Tribble, R. H. Burch, and C. A. Gagliardi, Nucl. Instrum. Methods Phys. Res. A **285**, 441 (1989).

[28] R. E. Tribble, C. A. Gagliardi, and W. Liu, Nucl. Instrum. Methods Phys. Res. B **56/57**, 956 (1991).

[29] J. F. Ziegler, J. P. Biersack, and U. Littmark, *The Stopping and Range of Ions in Solids* (Pergamon, New York, 1985), and accompanying computer code SRIM, version 96.

[30] *IUCF Data Acquisition Software* IUCF Internal Report, Indiana University Cyclotron Facility, Bloomington, Indiana, 1988.

[31] J. P. Jeukenne, A. Lejeune, and C. Mahaux, Phys. Rev. C **16**, 80 (1977).

[32] L. Trache, A. Azhari, H. L. Clark, C. A. Gagliardi, Y.-W. Lui, A. M. Mukhamedzhanov, R. E. Tribble, and F. Carstoiu, Phys. Rev. C **58**, 2715 (1998).

[33] P. Bém, V. Burjan, V. Kroha, J. Novák, Š. Piskoř, E. Šimečková, J. Vincour, C. A. Gagliardi, A. M. Mukhamedzhanov, and R. E. Tribble, Phys. Rev. C **62**, 024320 (2000).

[34] M. Rhoades-Brown, M. McFarlane, and S. Pieper, Phys. Rev. C **21**, 2417 (1980); **21**, 2436 (1980).

[35] I. J. Thompson, Comput. Phys. Rep. **7**, 167 (1988).

[36] M. N. Harakeh, J. Van Popta, A. Saha, and R. H. Siemssen, Nucl. Phys. **A344**, 15 (1980).

[37] A. M. Mukhamedzhanov and N. K. Timofeyuk, Yad. Fiz. **51**, 679 (1990) [Sov. J. Nucl. Phys. **51**, 431 (1990)].

[38] R. W. Kavanagh, Nucl. Phys. **15**, 411 (1960).